ACS APPLIED MATERIALS & INTERFACES

www.acsami.org

Research Article

Enhancing Reversible Hydrogen Storage Performance of $LiBH_4$ Catalyzed by N-Doped Carbon Nanosheet Networks Embedded with Co Nanoparticles

Wei Chen,[§] Yukun Liu,[§] Chaoqun Li, Yuchen Pang, Xuebin Yu,* and Guanglin Xia*

Cite This: *ACS Appl. Mater. Interfaces* 2025, 17, 50603−50611

Read Online

ACCESS | Metrics & More | Article Recommendations | Supporting Information

ABSTRACT: $LiBH_4$ is one of the most promising candidates for onboard solid-state hydrogen storage. Nevertheless, the implementation of this material in practical systems is limited due to its high operational temperature, slow kinetic behavior, and compromised reversible capacity. Herein, N-doped carbon nanosheet networks embedded with Co nanoparticles (Co/N-CNSNs) are designed as functional scaffolds to improve the hydrogen storage performance of $LiBH_4$. Co NPs and the *in situ* formed CoB in Co/N-CNSNs during the initial hydrogen desorption process could catalytically weaken the B−H bonds in $LiBH_4$, resulting in the reduction of H dissociation energy to 0.34 and 0.31 eV, respectively, much lower than that of pure $LiBH_4$ (1.95 eV). Benefiting from the synergistic effect of the catalytic role of Co NPs and the *in situ* formed CoB and the nanoconfinement role of Co/N-CNSNs, 10.1 wt % hydrogen could be released from $LiBH_4$@Co/N-CNSNs at 300 °C within 180 min, while this value is decreased to only 1.5 wt % for bulk $LiBH_4$ under the identical condition. Moreover, the homogeneous molecular interaction between Co/N-CNSNs and $LiBH_4$ leads to the formation of σ-bonds between Li^+ and the nonconjugated lone pair electrons of pyridinic N and pyrrolic N, which enables Co/N-CNSNs to act as anchoring sites for inhibiting the grain growth of $LiBH_4$, contributing to improving its reversibility. Hence, $LiBH_4$ nanoconfined within Co/N-CNSNs demonstrates a reversible hydrogen storage capacity of 9.7 wt % at 300 °C, even after 10 cycles of hydrogen storage.

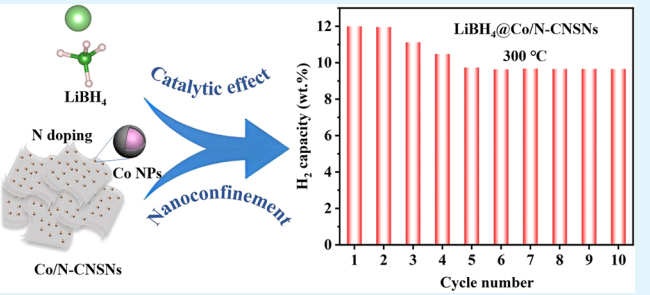

KEYWORDS: *hydrogen storage, lithium borohydride, nanoconfinement, catalysis, hydrogen*

INTRODUCTION

Hydrogen energy is widely regarded as the most promising candidate energy for the 21st century, while the safe and efficient storage of hydrogen limits its large-scale application.[1−6] The inherent safety and high hydrogen content of solid-state hydrogen storage materials, including metal hydrides and complex hydrides, have resulted in significant research interest.[7−15] Among them, lithium borohydride ($LiBH_4$) stands out as a highly promising candidate with a gravimetric hydrogen storage capacity reaching approximately 18.4 wt % and a volumetric density close to 121 kg/m^3.[16−18] However, ultrahigh kinetic barriers and thermodynamic stability lead to a high operating temperature of over 400 °C for dehydrogenation and even worse, a harsh condition of 600 °C and 35 MPa hydrogen pressure is required for reversible hydrogenation, which hinders its practical application.[19,20]

A plethora of strategies have been formulated with the objective of enhancing the hydrogen storage performance of $LiBH_4$. These strategies encompass the introduction of catalysts, nanoconfinement, and the preparation of a reactive hydride composite.[21−24] Particularly, transition-metal-based additives, including metal oxides, metal halides, and transition metals, are proved to be effective in improving the hydrogen storage performance of $LiBH_4$.[25−28] These additives could serve as effective catalysts for weakening B−H bonds or react with $LiBH_4$ for decreasing thermodynamic stability during the hydrogen desorption process, hence enhancing the hydrogen release performance of $LiBH_4$. For example, by the introduction of cobalt-based catalysts, the peak hydrogen desorption temperature of $LiBH_4$ is lowered by more than 90 °C, which could be attributed to the catalytic effect of the *in situ* formed CoB.[29,30] However, the catalytic mechanism of Co-based catalysts still remains unclear, and the reversibility of $LiBH_4$ is still inhibited due to the particle agglomeration of $LiBH_4$ or its dehydrogenation products under high temperature during the reversible hydrogen storage process. Nanoconfinement *via* confining $LiBH_4$ particles into a porous matrix at the nanoscale could suppress particle agglomeration,

Received: April 27, 2025
Revised: August 23, 2025
Accepted: August 24, 2025
Published: August 28, 2025

https://doi.org/10.1021/acsami.5c08381
ACS Appl. Mater. Interfaces 2025, 17, 50603−50611

enhance reaction kinetics, and improve reversible hydrogen storage performance simultaneously.[31−33] For this reason, the combination of catalysis and nanoconfinement is employed to further improve the hydrogen storage performance of $LiBH_4$.[34−36] The hydrogen desorption capacity of $LiBH_4$ nanoconfined into porous carbon decorated with CoNi catalyst at 350 °C within 100 min is 2 times higher than that without CoNi catalyst under identical conditions, which confirms the synergetic effect of catalysis and nanoconfinement in enhancing the hydrogen storage performance of $LiBH_4$.[37] Although various metal-based catalysts have been introduced to improve reversible hydrogen storage performance of nanoconfined $LiBH_4$, the operating temperature for hydrogen desorption and adsorption is still higher than 320 °C owing to the weak catalytic effect of these catalysts. More importantly, the reversibility of nanoconfined $LiBH_4$ is still poor, which could be attributed to the lack of control over the particle agglomeration of $LiBH_4$ even under the nanoconfinement role of a porous matrix.

Herein, N-doped carbon nanosheet networks embedded with Co nanoparticles (denoted as Co/N-CNSNs) were designed for the nanoconfinement of $LiBH_4$ *via* the typical solution impregnation method. During the initial hydrogen desorption process, Co nanoparticles (NPs) are *in situ* transformed into CoB NPs. Notably, when catalyzed by Co and CoB NPs, the average B−H bond length in $LiBH_4$ is extended from 1.24 to 1.47 and 1.48 Å, respectively, and it hence results in a significant reduction of H dissociation energy down to 0.34 and 0.31 eV, much lower than that of $LiBH_4$ (1.95 eV), which demonstrates the superior catalytic effect of Co and CoB NPs. Owing to the synergetic effect of catalytic role and nanoconfinement of Co/N-CNSNs, a hydrogen desorption capacity of 10.1 wt % is achieved for $LiBH_4$@Co/N-CNSNs at 300 °C within 180 min, which is 6.7 times higher than that of bulk $LiBH_4$ under the identical condition. In addition, the molecular interaction between the pyridinic and pyrrolic N sites uniformly distributed in Co/N-CNSNs and $LiBH_4$ leads to the formation of σ-bonds between Li^+ and the nonconjugated lone pair electrons of pyridinic N and pyrrolic N, which enables Co/N-CNSNs to act as anchoring sites for inhibiting the grain growth of $LiBH_4$, contributing to improving its reversibility. As a result, a reversible hydrogen storage capacity of 9.7 wt %, maintaining 81% of its initial capacity, is achieved for $LiBH_4$ nanoconfined in Co/N-CNSNs at a low temperature of 300 °C after 10 cycles of hydrogen adsorption and desorption process.

MATERIALS AND METHODS

Synthesis of ZIF-8. ZIF-8 was synthesized based on a previously established procedure.[38] Briefly, 1.07 g of $Zn(NO_3)_2{\cdot}6H_2O$ and 2.37 g of 2-methylimidazole were each dissolved in 25 mL of methanol, respectively. The two solutions were combined and stirred continuously at ambient temperature for 24 h. The resultant product after washing with methanol 3 times and vacuum-drying at 80 °C for 12 h was ZIF-8.

Synthesis of Co/N-CNSNs. 800 mg of ZIF-8 and 1200 mg of $Co(NO_3)_2{\cdot}6H_2O$ were dissolved into 50 mL of deionized water and kept stirring for 24 h. Subsequently, the products were washed by deionized water 3 times and then freeze-dried for 72 h to obtain 2-MI-LDHs. This intermediate was subsequently pyrolyzed at 900 °C for 2 h in a nitrogen atmosphere using a heating rate of 5 °C min^{-1}. The obtained product was then immersed in 5 wt % HCl solution and kept stirring for 24 h. After washing with deionized water 3 times and freeze-drying process, Co/N-CNSNs were obtained.[39]

Synthesis of $LiBH_4$@Co/N-CNSNs. The nanoconfinement of $LiBH_4$ into Co/N-CNSNs was performed by a simple solution infiltration method.[40] Typically, 22 mg of Co/N-CNSNs was dispersed in 5 mL of THF. Then, 0.5 mL of a 2 mol L^{-1} $LiBH_4$/THF solution was introduced under an argon atmosphere. The mixture was subjected to ultrasonication for 30 min to promote uniform dispersion and intimate contact between $LiBH_4$ and the porous support. The suspension was subsequently vacuum-dried at 80 °C for 12 h to evaporate the solvent. The obtained product was denoted as $LiBH_4$@Co/N-CNSNs.

Synthesis of $LiBH_4$@N-CNSNs. To remove Co species, a portion of Co/N-CNSNs was treated with 8 mol L^{-1} HNO_3 under stirring for 24 h. After being washed 4 times with deionized water and vacuum-dried at 80 °C for 12 h, N-CNSNs were obtained. Nanoconfinement of $LiBH_4$ in N-CNSNs (denoted as $LiBH_4$@N-CNSNs) was prepared by following the same synthesis procedures as $LiBH_4$@Co/N-CNSNs except for the replacement of Co/N-CNSNs with N-CNSNs.

Synthesis of $LiBH_4$−Co/N-CNSNs. A composite material composed of $LiBH_4$ and Co/N-CNSNs in a 1:1 weight ratio was prepared *via* mechanical milling. The mixture was processed at 300 rpm for 2 h under an Ar atmosphere using a planetary ball mill (QM-3SP4, Nanjing Nanda Instrument Plant), maintaining a ball-to-powder mass ratio of approximately 50:1. In order to avoid the increase of the temperature during the ball-milling process, the process was paused for 5 min after every 15 min of milling. The product was labeled as $LiBH_4$−Co/N-CNSNs.

Characterization. The morphological features of the samples were examined by scanning electron microscopy (SEM, Shimadzu JEOL 7500FA) and transmission electron microscopy (TEM, JEOL JEM-2100F). Elemental distribution was analyzed using energy-dispersive X-ray spectroscopy (EDS) coupled to TEM. Crystalline phases were identified using X-ray diffraction (XRD; Bruker D8 Advance) with Cu Kα radiation (50 kV, 30 mA). To prevent oxidation, all samples were mounted on XRD holders and sealed with Scotch tape in an argon-filled glovebox. Chemical bonding states were investigated using Fourier transform infrared spectroscopy (FTIR, Bruker Tensor 27). X-ray photoelectron spectroscopy (XPS) was performed using a Thermo Scientific K-Alpha+ instrument equipped with an Al Kα X-ray source.

Hydrogen absorption and desorption behaviors were quantitatively analyzed by using a high-pressure gas sorption analyzer (HPSA-auto). Desorption isotherms were collected at various fixed temperatures (300, 320, 340, and 360 °C) under static vacuum conditions over 3 h. For cyclic stability tests, the sample was first heated to 300 °C and held for 6 h at pressures below 0.001 bar. Rehydrogenation was then carried out at 400 °C under a hydrogen pressure of 100 bar for 10 h.

Theoretical Calculation. Spin-polarized density functional theory (DFT) calculations were executed using the Vienna Ab initio Simulation Package (VASP) with the projector-augmented wave (PAW) approach. Exchange-correlation effects were described *via* the Perdew−Burke−Ernzerhof (PBE) functional within the generalized gradient approximation (GGA). To account for van der Waals interactions at the $LiBH_4$/catalyst interface, the DFT-D3 dispersion correction with Becke−Johnson damping was employed. A 4 × 4 single-layer graphene slab was employed to simulate the graphene surface with pyridinic N and pyrrolic N sites modeled by substituting central carbon atoms with nitrogen atoms. A 2 × 2 CoB (100) slab and a 4 × 4 Co (001) slab were also constructed (Figure S1). A single $LiBH_4$ molecule was placed in the center of each slab to simulate the catalytic interaction. Additionally, a vacuum layer of 20 Å was added along the *z*-direction to prevent spurious interactions between periodic images. Nitrogen doping configurations (graphitic, pyridinic, and pyrrolic N) were systematically modeled on the basis of XPS characterization data. A plane-wave cutoff energy of 550 eV and a Γ-centered 4 × 4 × 1 *k*-point mesh were adopted after convergence tests, with energy and force convergence criteria set to 1 × 10^{-5} eV and 0.02 eV/Å, respectively. The hydrogen dissociation energy (specifically for breaking a B−H bond in $LiBH_4$) is calculated using density functional theory (DFT) *via* the following approach (eq 1)

https://doi.org/10.1021/acsami.5c08381
ACS Appl. Mater. Interfaces 2025, 17, 50603−50611

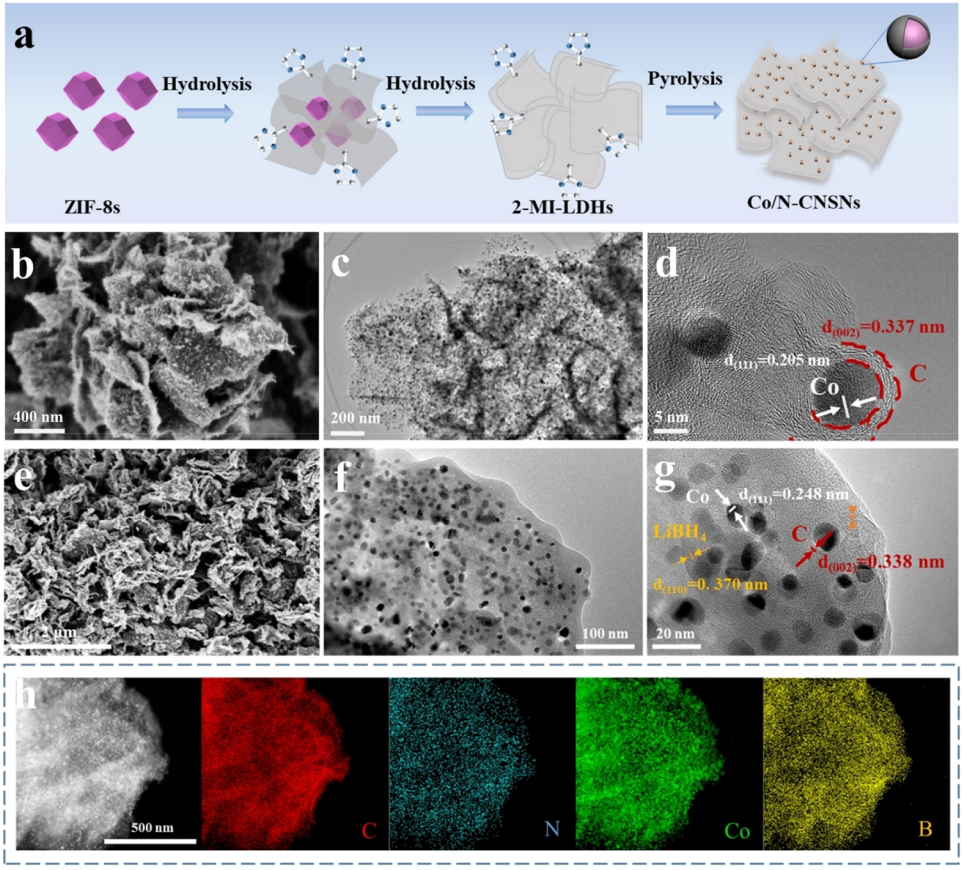

Figure 1. (a) Schematic illustration of the synthetic process of Co/N-CNSNs. (b) SEM, (c) TEM, and (d) HRTEM images of Co/N-CNSNs. (e) SEM, (f) TEM, and (g) HRTEM images of $LiBH_4$@Co/N-CNSNs. (h) STEM and the corresponding EDS elemental mapping images of $LiBH_4$@Co/N-CNSNs.

$$E_{diss} = E_H + E_{LiBH3} - E_{LiBH4} \quad (1)$$

where E_{diss} refers to the hydrogen dissociation energy, E_H is the energy of a hydrogen atom, E_{LiBH4} is the optimized energy of $LiBH_4$ on the catalyst surface, and E_{LiBH3} is the optimized energy of the system after removing one hydrogen atom from $LiBH_4$ on the catalyst surface.

RESULTS AND DISCUSSION

As schematically illustrated in Figure 1a, Co/N-CNSNs are synthesized *via* the hydrolysis and pyrolysis of ZIF-8, using a previously reported method. SEM image (Figure S2) shows that the particle size of ZIF-8 is around 50 nm with a polyhedral structure, which vanished in the subsequent hydrolysis process (Figure S3). After its carbonization under a N_2 atmosphere at 900 °C for 2 h and etching by HCl, flower-like N-doped carbon nanosheet networks embedded with Co nanoparticles (Co/N-CNSNs, Figure 1b) are obtained. X-ray diffraction (XRD) patterns in Figure S4 exhibit the diffraction peaks corresponding to Co in Co/N-CNSNs, which directly demonstrate the formation of Co nanoparticles (Co NPs) after the carbonization and etching process. TEM results in Figure 1c reveal the uniform distribution of Co NPs in Co/N-CNSNs. Additionally, the high-resolution TEM (HRTEM) image in Figure 1d presents a distinct lattice fringe with an interplanar distance of 0.205 nm, which is consistent with the (111) crystallographic plane of Co. Each Co NP, with a particle size ranging from 5 to 10 nm, is encapsulated by a carbon layer, which could inhibit particle agglomeration during the hydrogen storage process. According to the scanning TEM (STEM) and the relative EDS images of Co/N-CNSNs (Figure S5), the signals of Co and N correspond well with C, which further confirms the uniform distribution of Co NPs and N elements within Co/N-CNSNs.

The as-prepared flower-like Co/N-CNSNs were utilized as the nanoconfinement scaffolds with a mass ratio of 50 wt % to evaluate its effect on improving the hydrogen storage performance of $LiBH_4$. After the solvent infiltration process, the XRD pattern (Figure S6) continues to exhibit prominent diffraction peaks, corresponding to Co in the Co/N-CNSNs framework. However, no discernible peaks associated with $LiBH_4$ are detected, likely due to its amorphous state upon confinement. The presence of $LiBH_4$ is confirmed by FTIR analysis (Figure S7), which reveals characteristic $[BH_4]^-$ vibrational bands, specifically a bending mode at 1125 cm^{-1} and stretching modes at 2223, 2291, and 2384 cm^{-1}. These findings verify the successful incorporation of $LiBH_4$ into the porous structure of Co/N-CNSNs. SEM image of $LiBH_4$@Co/N-CNSNs (Figure 1e) demonstrates that the nanosheet structure of Co/N-CNSNs is well preserved after the solvent infiltration process, which confirms its structural stability. The nanoconfinement of $LiBH_4$ within Co/N-CNSNs could be clearly observed in the TEM image (Figure 1f). The HRTEM image (Figure 1g) displays typical lattice planes of 0.248, 0.338, and 0.370 nm, corresponding to the (111) plane of Co, (002) plane of C, and (110) plane of $LiBH_4$, respectively. Furthermore, the STEM image and the corresponding EDS mapping images (Figure 1h) provide additional confirmation of the uniform nanoconfinement of $LiBH_4$ in Co/N-CNSNs.

https://doi.org/10.1021/acsami.5c08381
ACS Appl. Mater. Interfaces 2025, 17, 50603−50611

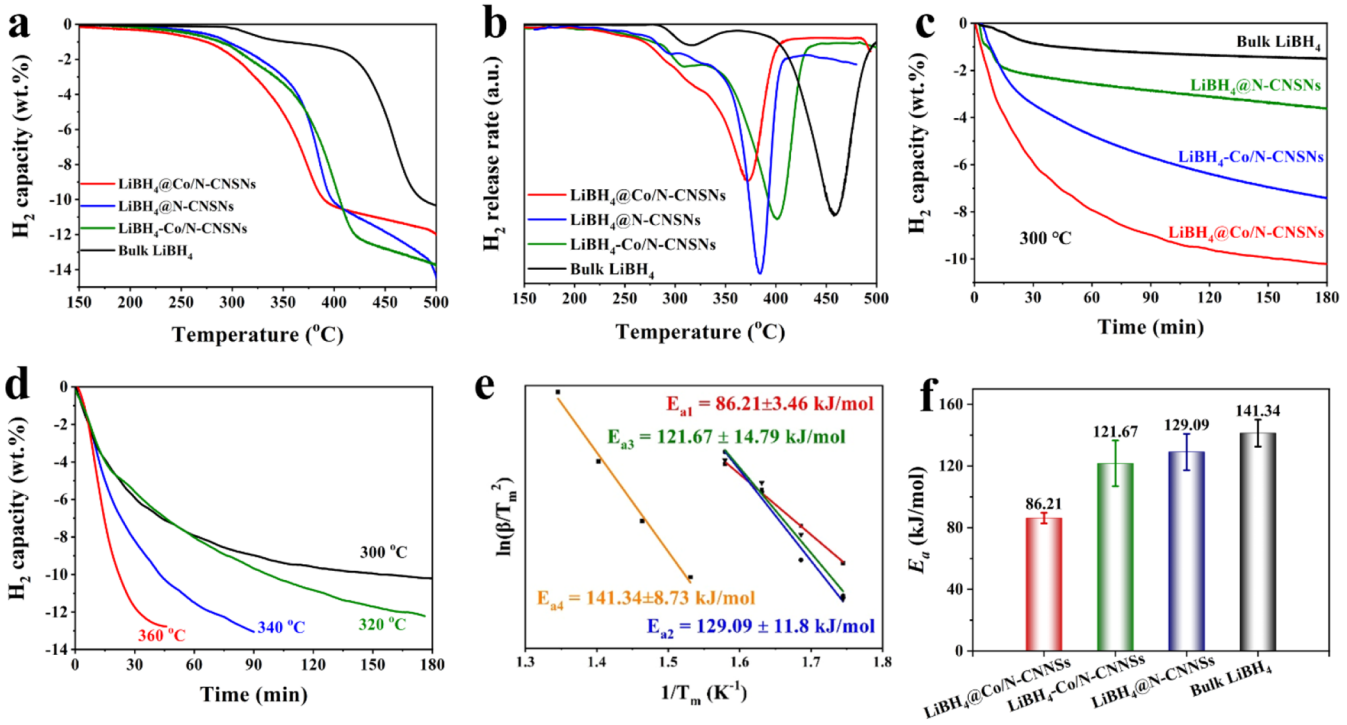

Figure 2. (a) TPD and (b) the related hydrogen release rate curves of bulk $LiBH_4$, $LiBH_4$−Co/N-CNSNs, $LiBH_4$@N-CNSNs, and $LiBH_4$@Co/N-CNSNs. (c) Isothermal hydrogen desorption kinetics of bulk $LiBH_4$, $LiBH_4$@N-CNSNs, $LiBH_4$−Co/N-CNSNs, and $LiBH_4$@Co/N-CNSNs at 300 °C. (d) Isothermal hydrogen desorption kinetics of $LiBH_4$@Co/N-CNSNs at various temperatures. (e) Arrhenius profiles and (f) the corresponding E_a of the hydrogen desorption of bulk $LiBH_4$, $LiBH_4$−Co/N-CNSNs, $LiBH_4$@N-CNSNs, and $LiBH_4$@Co/N-CNSNs.

The hydrogen desorption performance of $LiBH_4$@Co/N-CNSNs is subsequently investigated by the temperature-programmed desorption (TPD) method with a heating rate of 5 °C min^{-1} under an initial pressure lower than 0.001 bar (Figure 2a). For comparison, the ball-milled composite of $LiBH_4$ and Co/N-CNSNs ($LiBH_4$−Co/N-CNSNs), solvent-infiltrated $LiBH_4$ in N-CNSNs ($LiBH_4$@N-CNSNs), and bulk $LiBH_4$ are tested under identical conditions. As shown in Figure 2a,b, the onset hydrogen desorption temperature of bulk $LiBH_4$ is 284 °C with a main hydrogen desorption temperature reaching 460 °C. In comparison, the onset and peak hydrogen desorption temperature of $LiBH_4$−Co/N-CNSNs could be reduced to 227 and 401 °C, respectively, which serves as compelling evidence that Co/N-CNSNs act as effective catalysts, substantially boosting the hydrogen release capability of $LiBH_4$. It is interesting to note that the initial and peak hydrogen desorption temperatures are dramatically reduced to 216 and 372 °C, respectively, indicating the synergistic role of the catalytic effect and nanoconfinement of Co/N-CNSNs in facilitating the hydrogen desorption performance of $LiBH_4$. Moreover, the peak hydrogen desorption temperature of $LiBH_4$@N-CNSNs is reduced to 384, 12 °C higher than that of $LiBH_4$@Co/N-CNSNs, which further confirms the catalytic effect of Co in improving the hydrogen desorption performance of $LiBH_4$.

Isothermal hydrogen desorption performance of $LiBH_4$@Co/N-CNSNs is performed at various temperatures ranging from 300 to 360 °C to further verify the effect of Co/N-CNSNs in improving the hydrogen desorption kinetics of $LiBH_4$. As shown in Figure 2c, bulk $LiBH_4$ releases only 1.5 wt % hydrogen over 180 min at 300 °C, owing to its strong thermodynamic stability and inherently slow desorption kinetics. By comparison, 7.4 wt % could be released from $LiBH_4$−Co/N-CNSNs under the same condition (Figure 2d), which confirms the efficient catalytic role of Co/N-CNSNs in facilitating the hydrogen desorption of $LiBH_4$. Interestingly, 10.1 wt % hydrogen could be released from $LiBH_4$@Co/N-CNSNs at 300 °C in 180 min, highlighting the combined benefits of catalytic activity and nanoscale confinement provided by the Co/N-CNSNs support. To further identify the active catalytic species within the composite, through its infiltration into N-CNSNs, only 3.6 wt % hydrogen could be released from $LiBH_4$@N-CNSNs in 180 min at 300 °C, indicating the excellent catalytic effect of Co in enhancing the hydrogen desorption kinetics of $LiBH_4$. Furthermore, $LiBH_4$@Co/N-CNSNs could release 13.1 wt % hydrogen at 360 °C within a duration of 45 min (Figure 2d), which is approaching the theoretical hydrogen storage capacity of $LiBH_4$. In strong contrast, bulk $LiBH_4$ releases only 6.1 wt % hydrogen over 180 min, even when the temperature is elevated to 380 °C.

To quantitatively interpret the enhancement of Co/N-CNSNs in improving the hydrogen desorption kinetics of $LiBH_4$, the apparent activation energies (E_a) for hydrogen desorption are determined using the Arrhenius method based on isothermal hydrogen desorption curves of $LiBH_4$@Co/N-CNSNs (Figure 2d), bulk $LiBH_4$ (Figure S8), $LiBH_4$−Co/N-CNSNs (Figure S9), and $LiBH_4$@N-CNSNs (Figure S10). As shown in Figure 2e, by fitting the experimentally obtained curves at various temperatures, E_a for $LiBH_4$@Co/N-CNSNs is calculated to be 86.21 kJ mol^{-1} (Figure 2f), much lower than that of bulk $LiBH_4$ (141.34 kJ mol^{-1}), $LiBH_4$−Co/N-CNSNs (121.67 kJ mol^{-1}), and $LiBH_4$@N-CNSNs (129.09 kJ mol^{-1}). This result quantitatively demonstrates that the hydrogen desorption kinetics of $LiBH_4$ are significantly enhanced due to the synergistic effect of catalysis and nanoconfinement of Co/N-CNSNs.

https://doi.org/10.1021/acsami.5c08381
ACS Appl. Mater. Interfaces 2025, 17, 50603−50611

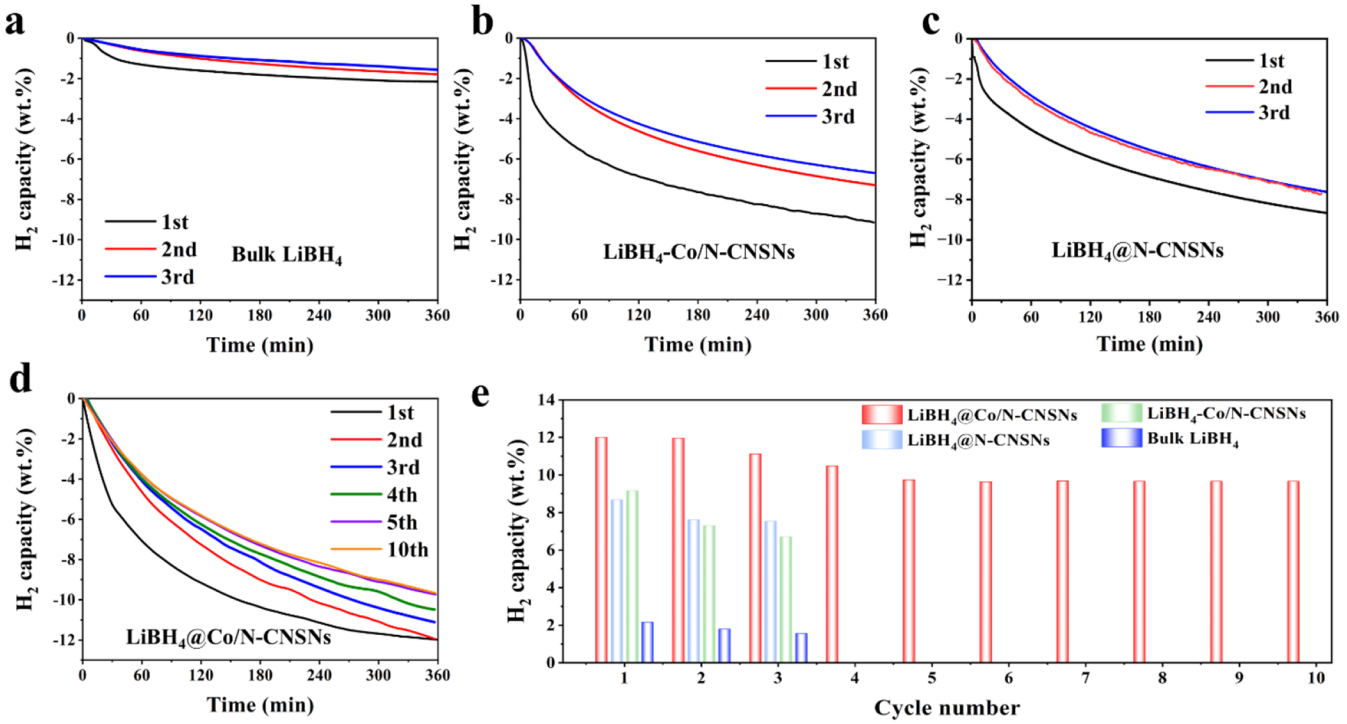

Figure 3. Cyclic hydrogen desorption performance of (a) bulk $LiBH_4$, (b) $LiBH_4$−Co/N-CNSNs, (c) $LiBH_4$@N-CNSNs, and (d) $LiBH_4$@Co/N-CNSNs at 300 °C. (e) The cycling capacity and capacity retention of $LiBH_4$@Co/N-CNSNs, with $LiBH_4$−Co/N-CNSNs, $LiBH_4$−Co/N-CNSNs, and bulk $LiBH_4$ included for comparison.

Owing to the phase separation of the hydrogen desorption products and the thermostability of as-formed B, the reversibility of $LiBH_4$ is another important parameter for its practical application; hence, the reversibility of $LiBH_4$@Co/N-CNSNs is further verified. Cycling hydrogen storage performance of the samples is performed under vacuum at 300 °C for 360 min for hydrogen desorption and under 100 bar hydrogen pressure at 400 °C for 600 min for hydrogen adsorption. As shown in Figure 3a, due to the high thermostability of $LiBH_4$, only 2.2 wt % hydrogen could be released from commercial $LiBH_4$ in the first cycle, and the capacity is further reduced to 1.6 wt % in the third cycle. In comparison, with the introduction of Co/N-CNSNs through ball milling, 9.2 wt % hydrogen could be released from $LiBH_4$−Co/N-CNSNs for the first cycle (Figure 3b), which could be attributed to the catalytic effect of Co/N-CNSNs. A capacity of 6.7 wt %, corresponding to 72.8% of the initial capacity, could be maintained after 3 cycles of the hydrogen adsorption and desorption process. In strong contrast, $LiBH_4$@Co/N-CNSNs could release 12.0 and 10.7 wt % hydrogen under the identical condition (Figure 3d) in the first and third hydrogen desorption cycles, respectively. More importantly, $LiBH_4$@Co/N-CNSNs demonstrate excellent cycling stability, maintaining a reversible capacity of 9.7 wt % even after ten successive cycles of hydrogen uptake and release (Figure 3e), corresponding to 81% of the initial capacity, which directly confirms the synergistic effect of catalysis and nanoconfinement of Co/N-CNSNs in improving the cycling stability of $LiBH_4$. Compared with the previously reported nanoconfined $LiBH_4$ system (Table S1), the operating temperature, the cycle number, and the reversible capacity of $LiBH_4$@Co/N-CNSNs are among the best. In addition, 9.2 wt % hydrogen could be released from $LiBH_4$@N-CNSNs in the first cycle, and it also could be well preserved to be 7.5 wt % after 3 cycles of the hydrogen adsorption and desorption process (Figure 3c), confirming the effect of nanoconfinement in enhancing the cycling stability of $LiBH_4$.

In order to explore the reaction mechanism of hydrogen storage enhancement of $LiBH_4$@Co/N-CNSNs, XRD is utilized to verify the products at different hydrogen sorption stages. As shown in Figure 4a, the diffraction peaks of Co are weakened during the cycling hydrogen storage process. New diffraction peaks assigned to CoB could be observed in the XRD patterns after the initial hydrogen desorption process, which demonstrates that Co NPs react with $LiBH_4$ during the hydrogen desorption process. The existence of CoB also could be verified by XPS measurement. The fitting peaks of binding energy at 778.7 and 793.5 eV in Co 2*p*XPS spectra (Figure 4b) are attributed to CoB, which provides additional evidence for the formation of CoB upon the hydrogen desorption process.[41] The binding energy located at 397.7, 399.3, and 401.8 eV in high-resolution XPS spectra of N 1*s* (Figure 4c) could be indexed to pyridinic N, pyrrolic N, and graphitic N, respectively.[42] According to previous reports, the existence of N in carbon scaffolds could catalytically improve the hydrogen desorption performance of $LiBH_4$;[43] as a result, under the catalytic effect of Co NPs and N-doping, the hydrogen desorption kinetics of $LiBH_4$@Co/N-CNSNs and $LiBH_4$−Co/N-CNSNs are significantly improved. Nevertheless, the XPS binding energy of as-formed CoB and N-doping could be observed in the subsequent rehydrogenation and 10th hydrogenation process (Figure 4b,c). The stable presence of CoB and N-doping could catalytically enhance the hydrogen storage performance of $LiBH_4$, corresponding well with the cycling results. Moreover, due to the pyrolysis of pyridinic N and the decomposition of graphitic N into pyrrolic N under high temperature,[44,45] the content of graphitic N and pyridinic

https://doi.org/10.1021/acsami.5c08381
ACS Appl. Mater. Interfaces 2025, 17, 50603−50611

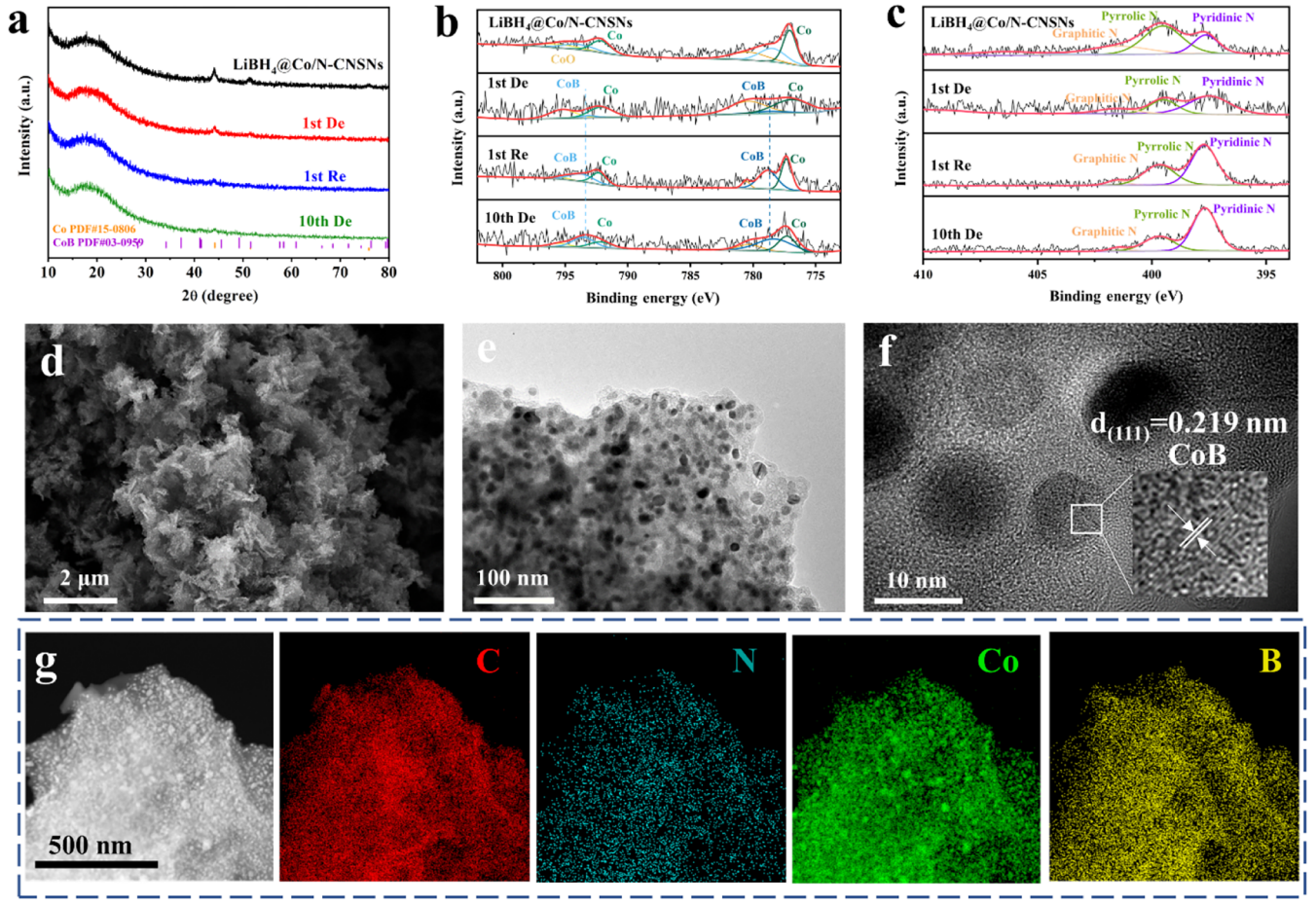

Figure 4. (a) XRD patterns of $LiBH_4$@Co/N-CNSNs at different hydrogen sorption stages. High-resolution XPS spectra of (b) Co 2*p* and (c) N 1*s* $LiBH_4$@Co/N-CNSNs at different hydrogen sorption stages. (d) SEM, (e) TEM, and (f) HRTEM images of $LiBH_4$@Co/N-CNSNs after the first hydrogen desorption process. (g) STEM and the relative EDS elemental mapping images of $LiBH_4$@Co/N-CNSNs after the first hydrogen desorption process.

N is reduced with the increase of pyrrolic N content after the cycling hydrogen storage test.

The morphology of $LiBH_4$@Co/N-CNSNs after the hydrogen desorption process is further revealed by SEM and TEM. As evidenced by SEM in Figure 4d,e, the flower-like carbon nanosheet networks of $LiBH_4$@Co/N-CNSNs are well maintained after the hydrogen desorption process, and the uniform distribution of dehydrogenation products could also be clearly observed in the TEM image, which demonstrates the structural stability of the nanoconfined sample. The HRTEM image (Figure 4f) reveals a lattice fringe spacing of 0.219 nm, corresponding to the (111) crystallographic plane of CoB, corresponding well with the XRD and XPS results. The STEM image and the corresponding EDS mapping images (Figure 4g) confirm the uniform distribution of B of the dehydrogenation products and C, N, and Co of the scaffolds, providing additional evidence for the effect of nanoconfinement in restricting the particle agglomeration and hence enhancing hydrogen storage performance of $LiBH_4$.

Systematic density functional theory (DFT) calculations are conducted to verify the catalytic effect of Co NPs and the N element in improving the hydrogen desorption performance of $LiBH_4$. Charge density differences of $LiBH_4$ are calculated in four configurations: (1) pure carbon, (2) carbon with 1 graphitic N, (3) carbon with 2 pyridinic N and 1 pyrrolic N, and (4) carbon with 3 pyridinic N. As shown in Figure 5a, after the nanoconfinement of $LiBH_4$ within Co/N-CNSNs, there is a noticeable accumulation of electrons near pyrrolic N and pyridinic N sites, whereas no obvious electron transfer could be observed near C and graphitic N, which could be attributed to the formation of σ-bonds between Li^+ and the nonconjugated lone pair electrons of pyridinic N as well as the partially localized electrons of pyrrolic N. The observed hybridization between the Li *s* and N $2p_x$ orbitals (Figure S11), as well as the significant electron accumulation at the Li−N interface (Figure 5a), provides additional evidence for this conclusion. The adsorption energies for $LiBH_4$ on pyridinic N and pyrrolic N are calculated to be −1.71 and −1.17 eV, respectively, much lower than those observed on pure carbon (−0.46 eV) and graphitic N (−0.37 eV). This substantial reduction in adsorption energy indicates that both pyridinic N and pyrrolic N in Co/N-CNSNs could act as anchoring sites for $LiBH_4$, which could inhibit the grain growth of $LiBH_4$ during cycling hydrogen storage processes and hence contribute to improving its reversible hydrogen storage performance.

Additionally, structural optimization through DFT calculations is carried out to reveal the catalytic mechanism of Co NPs and the as-formed CoB NPs in enhancing the hydrogen desorption of $LiBH_4$. Notably, upon exposure to Co NPs, the mean B−H bond length in $LiBH_4$ elongates from 1.24 to 1.47 Å under the catalysis of Co NPs. Furthermore, the H

https://doi.org/10.1021/acsami.5c08381
ACS Appl. Mater. Interfaces 2025, 17, 50603−50611

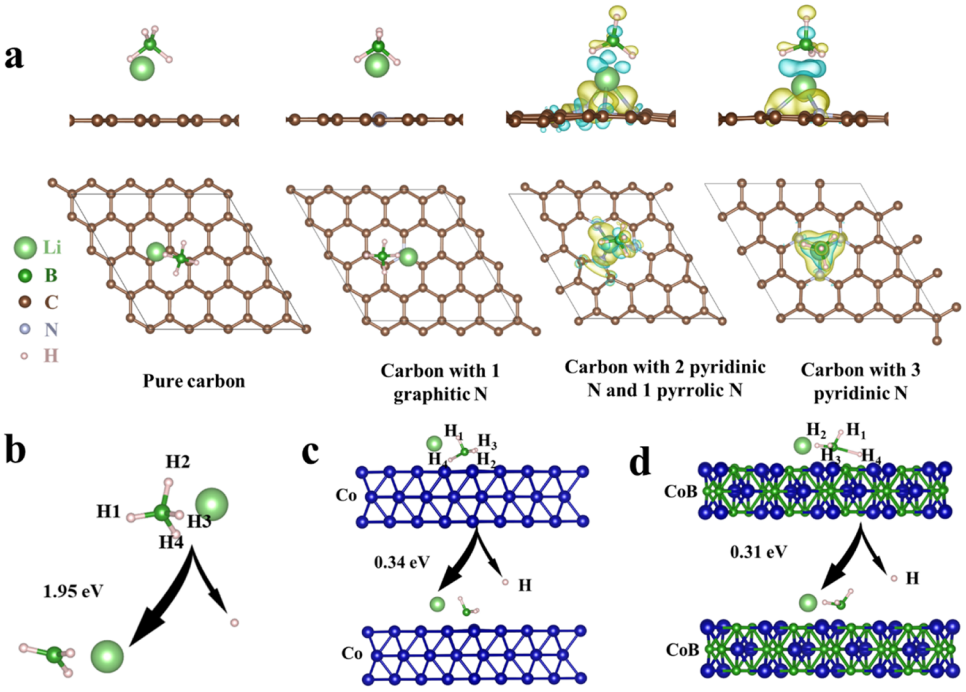

Figure 5. (a) Optimized adsorption configuration and corresponding charge density difference of $LiBH_4$ under the presence of pure carbon, carbon with 1 graphitic N, carbon with 2 pyridinic N and 1 pyrrolic N, and carbon with 3 pyridinic N, respectively. The charge density differences in (a) are plotted with an isovalue of 0.002 e·Bohr^{-3}. The yellow color represents the aggregation of the electron, and the blue color represents the loss of the electron. Changes in the hydrogen dissociation structure and energy from $LiBH_4$ (b) and $LiBH_4$ under the catalysis of (c) Co NPs and (d) CoB, respectively.

dissociation energy (E_{diss}) is calculated to be as high as 1.95 eV (Figure 5b) for $LiBH_4$, and this value could be dramatically reduced to 0.34 eV (Figure 5c) under the catalysis of Co NPs, which theoretically proves the catalytic effect of Co NPs in improving the hydrogen desorption performance of $LiBH_4$. Interestingly, after the formation of CoB upon the hydrogen storage process, the mean B−H bond length in $LiBH_4$ further elongates to 1.48 Å, and the H dissociation energy is further reduced to 0.31 eV (Figure 5d). Further charge density difference analysis (Figure S12) reveals that the bonding electrons between B and H tend to transfer toward the Co−H bond, indicating an electron redistribution induced by Co. Combined with the fact that the B site can coadsorb H^- species together with Co and simultaneously donate electrons to Li^+ to weaken the electron donation from Li to the $[BH_4]^-$ group and further destabilize the B−H bond, these findings demonstrate the synergistic catalytic effect of Co and B sites on the CoB surface in promoting $LiBH_4$ dehydrogenation. These results theoretically demonstrate the excellent catalytic performance of Co/N-CNSNs in enhancing the hydrogen desorption performance of $LiBH_4$ during cycling tests.

CONCLUSIONS

In this work, a novel Co nanoparticle-modified N-doped carbon nanosheet is fabricated *via* the hydrolysis of ZIF-8 and its subsequent carbonization to eliminate the kinetic sluggishness and poor reversibility of $LiBH_4$. The average B−H bond length in $LiBH_4$ increases from 1.24 to 1.47 and 1.48 Å under the catalysis of Co NPs and the *in situ* formed CoB during the initial cycle of the hydrogen storage process, respectively. This structural change leads to a reduction of the H dissociation energy to 0.34 and 0.31 eV, respectively, much lower than that of pure $LiBH_4$ (1.95 eV). Therefore, based on the synergistic effect of the catalytic role of Co NPs and the *in situ* formed CoB and the nanoconfinement role of Co/N-CNSNs, E_a for the hydrogen desorption of $LiBH_4$@Co/N-CNSNs is dramatically reduced to 86.21 kJ mol^{-1}. More importantly, the interaction between Co/N-CNSNs and $LiBH_4$ leads to the formation of σ-bonds between Li^+ and the nonconjugated lone pair electrons of pyridinic N and pyrrolic N. Hence, Co/N-CNSNs could act as anchoring sites for inhibiting the grain growth of $LiBH_4$ during the cycling hydrogen storage process, which contributes to improving its reversibility. As a result, a reversible capacity of 9.7 wt %, corresponding to 81% of the initial capacity, is achieved for $LiBH_4$@Co/N-CNSNs at 300 °C after 10 cycles of the hydrogen adsorption and desorption process.

ASSOCIATED CONTENT

Supporting Information

The Supporting Information is available free of charge at https://pubs.acs.org/doi/10.1021/acsami.5c08381.

Catalyst slab models constructed for DFT calculations; SEM images of ZIF-8s and 2-MI-LDHs; XRD patterns, STEM, and the relative EDS elemental mapping images of Co/N-CNSNs; XRD patterns and FTIR spectrum of $LiBH_4$@Co/N-CNSNs; isothermal hydrogen desorption curves of bulk $LiBH_4$, $LiBH_4$−Co/N-CNSNs, and $LiBH_4$@N-CNSNs at different temperatures; projected density of states (PDOS) analysis of $LiBH_4$ on pyrrolic N and pyridinic N sites; charge density difference of $LiBH_4$ under the presence of CoB (PDF)

https://doi.org/10.1021/acsami.5c08381
ACS Appl. Mater. Interfaces 2025, 17, 50603−50611

AUTHOR INFORMATION

Corresponding Authors

Xuebin Yu − *College of Smart Materials and Future Energy, Fudan University, Shanghai 200433, China;* orcid.org/0000-0002-4035-0991; Email: yuxuebin@fudan.edu.cn

Guanglin Xia − *College of Smart Materials and Future Energy, Fudan University, Shanghai 200433, China;* orcid.org/0000-0002-3493-4309; Email: xiaguanglin@fudan.edu.cn

Authors

Wei Chen − *College of Smart Materials and Future Energy, Fudan University, Shanghai 200433, China; Zhejiang Baima Lake Laboratory Co., Ltd., Hangzhou 310051, China*

Yukun Liu − *College of Smart Materials and Future Energy, Fudan University, Shanghai 200433, China*

Chaoqun Li − *College of Smart Materials and Future Energy, Fudan University, Shanghai 200433, China*

Yuchen Pang − *College of Smart Materials and Future Energy, Fudan University, Shanghai 200433, China*

Complete contact information is available at: https://pubs.acs.org/10.1021/acsami.5c08381

Author Contributions

[§]W.C. and Y.L. contributed equally to this work.

Notes

The authors declare no competing financial interest.

ACKNOWLEDGMENTS

This work was partially supported by the National Key R&D Program of China (No. 2021YFB3802400), the National Natural Science Foundation of China (Nos. U2130208, 22279020, and 52301264), and the Science and Technology Commission of Shanghai Municipality (Nos. 22ZR1406500 and 23ZR1406500).

REFERENCES

(1) Schlapbach, L.; Züttel, A. Hydrogen-storage materials for mobile applications. *Nature* **2001**, *414* (6861), 353−358.

(2) Yu, X.; Tang, Z.; Sun, D.; Ouyang, L.; Zhu, M. Recent advances and remaining challenges of nanostructured materials for hydrogen storage applications. *Prog. Mater. Sci.* **2017**, *88*, 1−48.

(3) Züttel, A. Materials for hydrogen storage. *Mater. Today* **2003**, *6* (9), 24−33.

(4) Liu, Y.; Zhong, K.; Luo, K.; Gao, M.; Pan, H.; Wang, Q. Size-dependent kinetic enhancement in hydrogen absorption and desorption of the Li−Mg−N−H system. *J. Am. Chem. Soc.* **2009**, *131* (5), 1862−1870.

(5) Zhang, X.; Liu, Y.; Ren, Z.; Zhang, X.; Hu, J.; Huang, Z.; Lu, Y.; Gao, M.; Pan, H. Realizing 6.7 wt% reversible storage of hydrogen at ambient temperature with non-confined ultrafine magnesium hydrides. *Energy Environ. Sci.* **2021**, *14* (4), 2302−2313.

(6) Zhang, H.; Xia, G.; Zhang, J.; Sun, D.; Guo, Z.; Yu, X. Graphene-Tailored Thermodynamics and Kinetics to Fabricate Metal Borohydride Nanoparticles with High Purity and Enhanced Reversibility. *Adv. Energy Mater.* **2018**, *8* (13), No. 1702975.

(7) Lai, Q.; Paskevicius, M.; Sheppard, D. A.; Buckley, C. E.; Thornton, A. W.; Hill, M. R.; Gu, Q.; Mao, J.; Huang, Z.; Liu, H. K.; et al. Hydrogen storage materials for mobile and stationary applications: current state of the art. *ChemSusChem* **2015**, *8* (17), 2789−2825.

(8) Ren, L.; Li, Y.; Zhang, N.; Li, Z.; Lin, X.; Zhu, W.; Lu, C.; Ding, W.; Zou, J. Nanostructuring of Mg-based hydrogen storage materials: recent advances for promoting key applications. *Nano Micro Lett.* **2023**, *15* (1), No. 93.

(9) Jain, I.; Jain, P.; Jain, A. Novel hydrogen storage materials: A review of lightweight complex hydrides. *J. Alloys Compd.* **2010**, *503* (2), 303−339.

(10) Pang, Y.; Liu, Y.; Gao, M.; Ouyang, L.; Liu, J.; Wang, H.; Zhu, M.; Pan, H. A mechanical-force-driven physical vapour deposition approach to fabricating complex hydride nanostructures. *Nat. Commun.* **2014**, *5* (1), No. 3519.

(11) Liu, Y.; Du, H.; Zhang, X.; Yang, Y.; Gao, M.; Pan, H. Superior catalytic activity derived from a two-dimensional Ti3C2 precursor towards the hydrogen storage reaction of magnesium hydride. *Chem. Commun.* **2016**, *52* (4), 705−708.

(12) Zhang, X.; Ju, S.; Li, C.; Hao, J.; Sun, Y.; Hu, X.; Chen, W.; Chen, J.; He, L.; Xia, G.; et al. Atomic reconstruction for realizing stable solar-driven reversible hydrogen storage of magnesium hydride. *Nat. Commun.* **2024**, *15* (1), No. 2815.

(13) Wang, Y.; Chen, X.; Zhang, H.; Xia, G.; Sun, D.; Yu, X. Heterostructures built in metal hydrides for advanced hydrogen storage reversibility. *Adv. Mater.* **2020**, *32* (31), No. 2002647.

(14) Xia, G.; Tan, Y.; Chen, X.; Sun, D.; Guo, Z.; Liu, H.; Ouyang, L.; Zhu, M.; Yu, X. Monodisperse magnesium hydride nanoparticles uniformly self-assembled on graphene. *Adv. Mater.* **2015**, *27* (39), 5981−5988.

(15) Hu, J. W.; Chen, X.; Zhang, X.; Meng, Y.; Xia, G.; Yu, X.; Sun, D.; Fang, F. In situ construction of interface with photothermal and mutual catalytic effect for efficient solar-driven reversible hydrogen storage of MgH_2. *Adv. Sci.* **2024**, *11* (22), No. 2400274.

(16) Züttel, A.; Wenger, P.; Rentsch, S.; Sudan, P.; Mauron, P.; Emmenegger, C. $LiBH_4$ a new hydrogen storage material. *J. Power Sources* **2003**, *118* (1−2), 1−7.

(17) Yang, X.; Su, J.; Lu, X.; Kong, J.; Huo, D.; Pan, Y.; Li, W. Application and development of $LiBH_4$ hydrogen storage materials. *J. Alloys Compd.* **2024**, *1001*, No. 175174.

(18) Zhang, X.; Li, C.; Ye, J.; Hu, X.; Chen, W.; Fang, F.; Sun, D.; Liu, Y.; Yu, X.; Xia, G. Light-enabled reversible hydrogen storage of borohydrides activated by photogenerated vacancies. *J. Am. Chem. Soc.* **2025**, *147* (3), 2786−2796.

(19) Wu, M.; Gao, M.; Qu, S.; Liu, Y.; Sun, W.; Liang, C.; Zhang, X.; Li, Z.; Yang, Y.; Pan, H. $LiBH_4$ hydrogen storage system with low dehydrogenation temperature and favorable reversibility promoted by metallocene additives. *J. Energy Storage* **2023**, *72*, No. 108679.

(20) Xu, Y.; Zhou, Y.; Li, Y.; Ashuri, M.; Ding, Z. Engineering $LiBH_4$-Based Materials for Advanced Hydrogen Storage: A Critical Review of Catalysis, Nanoconfinement, and Composite Design. *Molecules* **2024**, *29* (23), No. 5774.

(21) Li, Z.; Wang, S.; Gao, M.; Xian, K.; Shen, Y.; Yang, Y.; Gao, P.; Sun, W.; Liu, Y.; Pan, H. Catalyzed $LiBH_4$ Hydrogen Storage System with In Situ Introduced Li_3BO_3 and V for Enhanced Dehydrogenation and Hydrogenation Kinetics as Well as High Cycling Stability. *ACS Appl. Energy Mater.* **2022**, *5* (1), 1226−1234.

(22) Gross, A. F.; Vajo, J. J.; Van Atta, S. L.; Olson, G. L. Enhanced Hydrogen Storage Kinetics of $LiBH_4$ in Nanoporous Carbon Scaffolds. *J. Phys. Chem. C* **2008**, *112* (14), 5651−5657.

(23) Plerdsranoy, P.; Utke, R. Confined $LiBH_4$−$LiAlH_4$ in nanopores of activated carbon nanofibers. *Int. J. Hydrogen Energy* **2015**, *40* (22), 7083−7092.

(24) Ding, Z.; Li, H.; Shaw, L. New insights into the solid-state hydrogen storage of nanostructured $LiBH_4$-MgH_2 system. *Chem. Eng. J.* **2020**, *385*, No. 123856.

(25) Li, Z.; Gao, M.; Wang, S.; Zhang, X.; Gao, P.; Yang, Y.; Sun, W.; Liu, Y.; Pan, H. In-situ introduction of highly active TiO for enhancing hydrogen storage performance of $LiBH_4$. *Chem. Eng. J.* **2022**, *433*, No. 134485.

(26) Xia, G. L.; Guo, Y. H.; Wu, Z.; Yu, X. B. Enhanced hydrogen storage performance of $LiBH_4$−Ni composite. *J. Alloys Compd.* **2009**, *479* (1), 545−548.

(27) Puszkiel, J.; Gasnier, A.; Amica, G.; Gennari, F. Tuning $LiBH_4$ for Hydrogen Storage: Destabilization, Additive, and Nanoconfinement Approaches. *Molecules* **2020**, *25* (1), No. 163.

(28) Yang, J.; Sudik, A.; Wolverton, C. Destabilizing $LiBH_4$ with a Metal (M = Mg, Al, Ti, V, Cr, or Sc) or Metal Hydride (MH_2 = MgH_2, TiH_2, or CaH_2). *J. Phys. Chem. C* **2007**, *111* (51), 19134−19140.
(29) Zhang, B. J.; Liu, B. H. Hydrogen desorption from $LiBH_4$ destabilized by chlorides of transition metal Fe, Co, and Ni. *Int. J. Hydrogen Energy* **2010**, *35* (14), 7288−7294.
(30) Cai, W.; Wang, H.; Jiao, L.; Wang, Y.; Zhu, M. Remarkable irreversible and reversible dehydrogenation of $LiBH_4$ by doping with nanosized cobalt metalloid compounds. *Int. J. Hydrogen Energy* **2013**, *38* (8), 3304−3312.
(31) Shao, J.; Xiao, X.; Fan, X.; Zhang, L.; Li, S.; Ge, H.; Wang, Q.; Chen, L. Low-temperature reversible hydrogen storage properties of $LiBH_4$: a synergetic effect of nanoconfinement and nanocatalysis. *J. Phys. Chem. C* **2014**, *118* (21), 11252−11260.
(32) Gosalawit-Utke, R.; Meethom, S.; Pistidda, C.; Milanese, C.; Laipple, D.; Saisopa, T.; Marini, A.; Klassen, T.; Dornheim, M. Destabilization of $LiBH_4$ by nanoconfinement in PMMA−co−BM polymer matrix for reversible hydrogen storage. *Int. J. Hydrogen Energy* **2014**, *39* (10), 5019−5029.
(33) Remhof, A.; Mauron, P.; Züttel, A.; Embs, J. P.; Łodziana, Z.; Ramirez-Cuesta, A. J.; Ngene, P.; de Jongh, P. Hydrogen Dynamics in Nanoconfined Lithiumborohydride. *J. Phys. Chem. C* **2013**, *117* (8), 3789−3798.
(34) Wang, S.; Gao, M.; Yao, Z.; Liu, Y.; Wu, M.; Li, Z.; Liu, Y.; Sun, W.; Pan, H. A nanoconfined-$LiBH_4$ system using a unique multifunctional porous scaffold of carbon wrapped ultrafine Fe_3O_4 skeleton for reversible hydrogen storage with high capacity. *Chem. Eng. J.* **2022**, *428*, No. 131056.
(35) Xu, G.; Zhang, W.; Zhang, Y.; Zhao, X.; Wen, P.; Ma, D. Fe_3O_4 nanoclusters highly dispersed on a porous graphene support as an additive for improving the hydrogen storage properties of $LiBH_4$. *RSC Adv.* **2018**, *8* (35), 19353−19361.
(36) Guo, Y.; Liu, Y.; Feng, L.; An, C.; Wang, Y. High-loading $LiBH_4$ Confined in Structurally Tunable Ni Catalyst-decorated Porous Carbon Scaffold for Fast Hydrogen Desorption. *Chem. - Asian J.* **2023**, *18* (7), No. e202300009.
(37) Ding, Y.; Li, C.; Zhang, X.; Chen, W.; Yu, X.; Xia, G. Spatial Confinement of Lithium Borohydride in Bimetallic CoNi-Doped Hollow Carbon Frameworks for Stable Hydrogen Storage. *ACS Appl. Mater. Interfaces* **2024**, *16* (38), 50717−50725.
(38) Lee, Y.-R.; Jang, M.-S.; Cho, H.-Y.; Kwon, H.-J.; Kim, S.; Ahn, W.-S. ZIF-8: A comparison of synthesis methods. *Chem. Eng. J.* **2015**, *271*, 276−280.
(39) Huang, X.; Zhang, Y.; Shen, H.; Li, W.; Shen, T.; Ali, Z.; Tang, T.; Guo, S.; Sun, Q.; Hou, Y. N-Doped Carbon Nanosheet Networks with Favorable Active Sites Triggered by Metal Nanoparticles as Bifunctional Oxygen Electrocatalysts. *ACS Energy Lett.* **2018**, *3* (12), 2914−2920.
(40) Liu, Y.; Chen, W.; Ju, S.; Yu, X.; Xia, G. Stable hydrogen storage of lithium borohydrides via the catalytic effect of Ni_2B induced by thermodynamic destabilization reaction. *J. Mater. Sci. Technol.* **2024**, *202*, 192−200.
(41) Yuan, H.; Wei, S.; Tang, B.; Ma, Z.; Li, J.; Kundu, M.; Wang, X. Self-Supported 3D Ultrathin Cobalt−Nickel−Boron Nanoflakes as an Efficient Electrocatalyst for the Oxygen Evolution Reaction. *ChemSusChem* **2020**, *13* (14), 3662−3670.
(42) Huang, H.; Yu, D.; Hu, F.; Huang, S.-C.; Song, J.; Chen, H.-Y.; Li, L. L.; Peng, S. Clusters Induced Electron Redistribution to Tune Oxygen Reduction Activity of Transition Metal Single-Atom for Metal−Air Batteries. *Angew. Chem., Int. Ed.* **2022**, *61* (12), No. e202116068.
(43) Gasnier, A.; Luguet, M.; Pereira, A. G.; Troiani, H.; Zampieri, G.; Gennari, F. C. Entanglement of N-doped graphene in resorcinol-formaldehyde: Effect over nanoconfined $LiBH_4$ for hydrogen storage. *Carbon* **2019**, *147*, 284−294.
(44) Zhao, D.; Sun, K.; Cheong, W. C.; Zheng, L.; Zhang, C.; Liu, S.; Cao, X.; Wu, K.; Pan, Y.; Zhuang, Z.; et al. Synergistically interactive pyridinic-N−MoP sites: identified active centers for enhanced hydrogen evolution in alkaline solution. *Angew. Chem.* **2020**, *132* (23), 9067−9075.
(45) Liu, J.; Song, P.; Ruan, M.; Xu, W. Catalytic properties of graphitic and pyridinic nitrogen doped on carbon black for oxygen reduction reaction. *Chin. J. Catal.* **2016**, *37* (7), 1119−1126.

https://doi.org/10.1021/acsami.5c08381
ACS Appl. Mater. Interfaces 2025, 17, 50603−50611